# nature nanotechnology

**Article** 

https://doi.org/10.1038/s41565-024-01697-z

# Very-large-scale-integrated high quality factor nanoantenna pixels

Received: 31 October 2023

Accepted: 15 May 2024

Published online: 03 July 2024

Check for updates

Varun Dolia ®¹ ⊠, Halleh B. Balch ®¹, Sahil Dagli¹, Sajjad Abdollahramezani¹, Hamish Carr Delgado ®¹, Parivash Moradifar¹, Kai Chang², Ariel Stiber ®¹, Fareeha Safir ®³, Mark Lawrence ®⁴ ⊠, Jack Hu ®³ ⊠ & Jennifer A. Dionne ®¹ ⊠

Metasurfaces precisely control the amplitude, polarization and phase of light, with applications spanning imaging, sensing, modulation and computing. Three crucial performance metrics of metasurfaces and their constituent resonators are the quality factor (Q factor), mode volume  $(V_m)$ and ability to control far-field radiation. Often, resonators face a trade-off between these parameters: a reduction in  $V_m$  leads to an equivalent reduction in Q, albeit with more control over radiation. Here we demonstrate that this perceived compromise is not inevitable: high quality factor, subwavelength  $V_m$  and controlled dipole-like radiation can be achieved simultaneously. We design high quality factor, very-largescale-integrated silicon nanoantenna pixels (VINPix) that combine guided mode resonance waveguides with photonic crystal cavities. With optimized nanoantennas, we achieve Q factors exceeding 1,500 with  $V_m$  less than 0.1  $(\lambda/n_{\rm air})^3$ . Each nanoantenna is individually addressable by free-space light and exhibits dipole-like scattering to the far-field. Resonator densities exceeding a million nanoantennas per cm<sup>2</sup> can be achieved. As a proof-of-concept application, we show spectrometer-free, spatially localized, refractive-index sensing, and fabrication of an 8 mm × 8 mm VINPix array. Our platform provides a foundation for compact, densely multiplexed devices such as spatial light modulators, computational spectrometers and in situ environmental sensors.

Photonic resonators are evaluated using two key metrics: quality factor (Q factor) and mode volume ( $V_m$ ). The Q factor measures temporal confinement of electromagnetic waves, indicated by the mode's linewidth.  $V_m$  quantifies the spatial concentration of the modes. Metasurfaces, arrays of nano-scale optical resonators, stand as some of the most recent and impactful innovations in photonics<sup>1-3</sup>. Owing to each resonator's ability to control the phase, amplitude, and polarization of light, metasurfaces can manipulate far-field radiation in a compact footprint. Particularly, metasurfaces have found applications in meeting the growing demand of platforms for wearable, deployable

or point-of-care scenarios such as health and environmental monitoring<sup>4-7</sup>, light detection and ranging systems<sup>8,9</sup>, wavefront shaping and imaging<sup>10-15</sup>, modulation<sup>16,17</sup>, computing<sup>18,19</sup> and computational spectrometry<sup>20,21</sup>. Metasurfaces have added another key metric to photonic resonators beyond Q factor and  $V_{\rm m}$ : the ability to control free-space radiation.

Plasmonic and Mie resonators, foundational elements of metasurfaces, confine light into subwavelength volumes and adeptly manipulate far-field radiation  $^{22-26}$ . However, these nanostructures often show modest Q factors (tens to hundreds) due to increased radiative

<sup>1</sup>Department of Materials Science and Engineering, Stanford University, Stanford, CA, USA. <sup>2</sup>Department of Electrical Engineering, Stanford University, Stanford, CA, USA. <sup>3</sup>Pumpkinseed Technologies, Palo Alto, CA, USA. <sup>4</sup>Department of Electrical and Systems Engineering, Washington University in St. Louis, St. Louis, MO, USA. ⊠e-mail: vdolia@stanford.edu; markl@wustl.edu; jack@pumpkinseed.bio; jdionne@stanford.edu

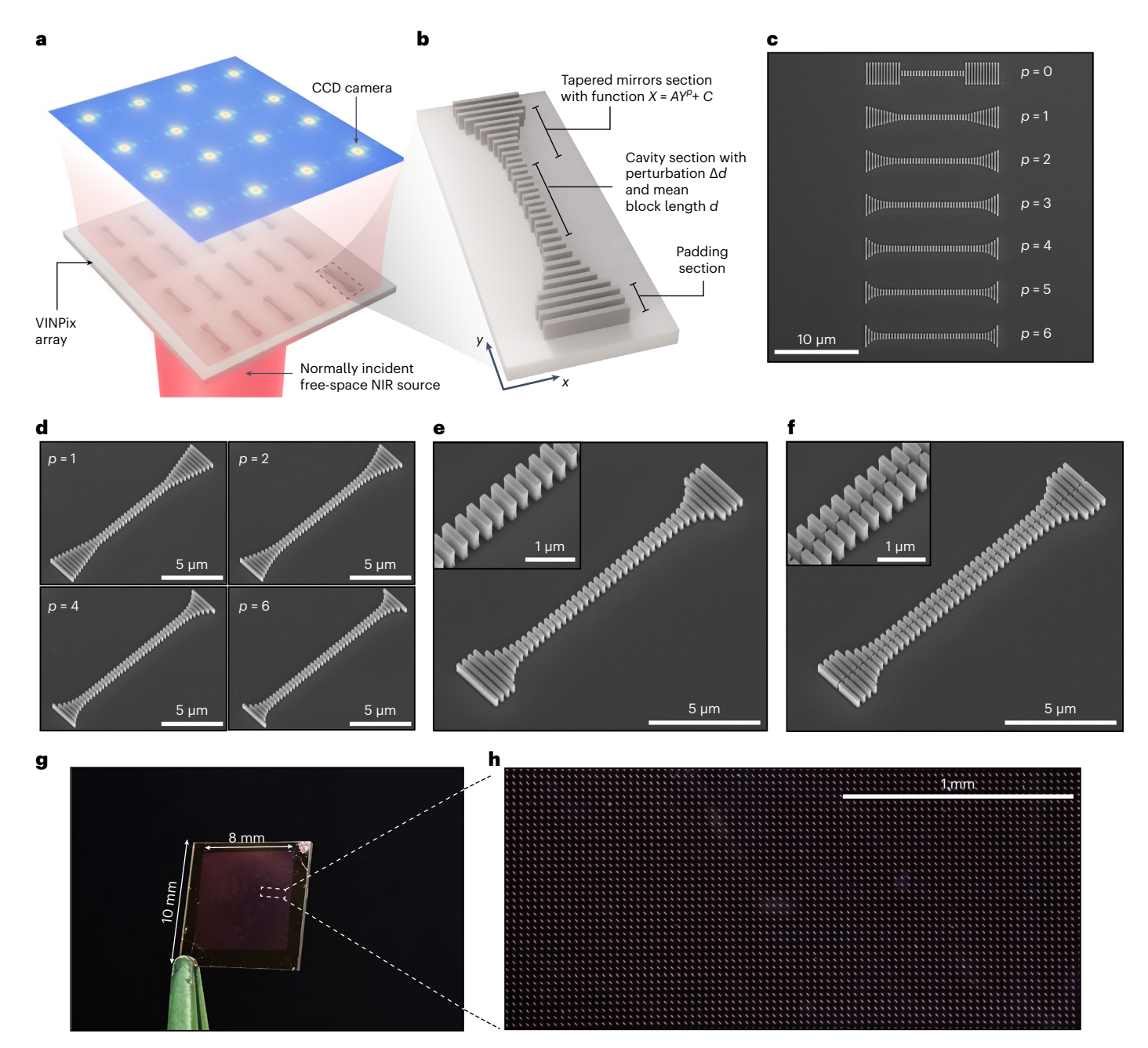


**Fig. 1** | **VINPix resonators. a**, Schematic of an array of individually addressable 15-μm-long high-Q photonic antennas (VINPix) made of Si nanoblocks on a sapphire substrate. The resonators are excited using a normally incident NIR laser source, and the scattered light is recorded using a camera or an imaging spectrometer. **b**, Representation of a VINPix's structural design, broken into three sections: a photonic cavity section, a tapered mirrors section and a padding mirrors section. **c**, Top view (SEM image) of VINPix resonators with different tapering functions—polynomials of order, p = 0-6 from top to bottom—without

any padding sections. **d**, Angled SEM images of VINPix without padding sections, and p=1,2,4 and 6, as labelled. **e**, Angled SEM image, with enlarged inset of the cavity section, of a representative 15- $\mu$ m-long VINPix consisting of a 7- $\mu$ m-long cavity section, 3- $\mu$ m-long tapered mirror sections and 1- $\mu$ m-long padding sections. **f**, Angled SEM image, with enlarged inset of the cavity section, of a slotted VINPix with a 70-nm-wide slot. **g**, A large-scale VINPix array patterned with VINPix resonators spanning an area of 8 mm  $\times$  8 mm on a 10 mm  $\times$  10 mm chip. **h**, Dark-field optical microscopy image of a small section of a VINPix array.

channels. Recently, high quality factor (high-Q) metasurfaces merging high-Q cavities with Mie antennas have emerged. These metasurfaces enable high-Q (>1,000), controlled far-field radiation, and wavefront control, operating on the principle of free-space excitation of guided mode resonances (GMRs) that scatter orthogonally as a dipole 7.11,27,28. Yet, maintaining high-Q in these structures often requires at least one translationally invariant dimension, rendering subwavelength mode volumes a challenge.

Meanwhile, high-Q photonic crystal defect cavities have demonstrated high-Q with subwavelength mode volumes  $(10^{-4}-10^{-1}(\lambda/n)^3)$ 

through in-plane band-gap confinements<sup>29–33</sup>. However, they scatter light arbitrarily with limited control over free-space radiation, as emission often spreads out in many directions, without a distinct or intended pattern. Whispering-gallery-mode resonators such as ring resonators, microtoroids and microspheres<sup>34–37</sup> achieve higher Q factors ranging from thousands to billions. However, these ultrahigh Q factor structures exhibit relatively large  $V_m$  values (on the order of a few to hundred cubic wavelengths). Additionally, they require fibres, prisms or grating-couplers to address wavevector mismatches due to their limited free-space coupling efficiencies. These results beg the

question: can optical resonators be designed to simultaneously provide high-Q, small  $V_m$  and controlled dipolar radiation?

In this Article, we present high-Q antennas that sculpt free-space light into subwavelength volumes while controlling far-field radiation with a dipole-like scattering profile. Merging high-QGMR waveguides<sup>7,11</sup> with photonic crystal cavities<sup>29</sup>, we design free-space subwavelength  $V_{\rm m}$ , high-Q resonators. Owing to their very-large-scale patterning (densities of >1 million antennas per cm<sup>2</sup>) and combination of distinct photonic elements integrated within a compact pixelated design, we term these nanoantennas very-large-scale-integrated silicon nanoantenna pixels (VINPix). Experimentally, we achieve Q factors as high as ~4,700 for individual VINPix resonators with free-space excitation. Incorporating a slot in our design, we predict deep subwavelength mode volumes ( $\sim 0.07 (\lambda/n_{\rm air})^3$ ) with experimental Q factors surpassing 1,500, showcasing heightened sensitivity to surrounding refractive-index variations. As a proof of concept, we create a dense VINPix array of 8mm×8mm and image local refractive-index variations for high-resolution and high-sensitivity spectrometer-free hyperspectral mapping.

# The VINPix resonator design

Figure 1a,b depicts our setup and the structural design of a VINPix. Our design comprises: (1) a photonic cavity section, (2) tapered photonic mirrors and (3) padding photonic mirrors. Figure 1c-f displays scanning electron microscopy (SEM) images of several antenna designs. All structures are based on 600-nm-tall Si nanoblocks on a sapphire substrate. Figure 1g,h shows large-scale arrays of these antennas. The first design feature of VINPix is its cavity section. The optical cavity supports bound modes that can be coupled to normally incident free-space light as GMRs by introducing a bi-periodic width perturbation,  $\Delta d$  (Supplementary Fig. 1). The introduction of subtle periodic perturbations in the waveguide cavity section bridges the wavevector mismatch between the incident light and the guided modes within the resonator (Supplementary Information)  $^{\rm 11,28,38-41}$ .

To achieve optical resonances in the near-infrared (NIR) telecommunication frequency range, we select the average block width, d, to be 600 nm (Supplementary Fig. 3). The bonding and anti-bonding GMRs of interest are at 207 THz and 262 THz, respectively, for normally incident light with an infinitely long waveguide cavity (Fig. 2a and Supplementary Fig. 1). The perturbation magnitude ( $\Delta d$ ) controls the lifetime (and Q factor) of the GMRs. Decreasing the perturbation increases the Q factor to as high as -240,000, with a 10 nm perturbation (Supplementary Fig. 4). The long resonant lifetime results in a strong -40-fold increase in the electric near-field enhancement (Fig. 2b). Taking into account the fabrication limitations,  $\Delta d$  was chosen to be 50 nm, unless specified otherwise.

The second design feature of the VINPix is the integration of photonic mirrors. Tapered photonic mirrors allow us to truncate the cavity length, that is, decrease the  $V_{\rm m}$ , while preserving Q factors through band-gap effects 42,43. Without mirrors, as the cavity length is reduced, the Q factor drops substantially due to radiation losses (Fig. 2c). For example, the Q factor drops from -12,000 to 600 when the cavity is shortened from semi-infinite to  $5~\mu {\rm m}$  without photonic mirrors. Here, we design nanoblocks of the same thickness but varying widths (d) as our individual mirror segments to create our tapered photonic mirrors. Figure 2d presents a simplified band structure for a mirror segment with d = 600 nm. The mode gap indicates the range of forbidden frequencies that are reflected by the mirror segment. A mirror segment's reflection strength is contingent on the relative positions of its bands and the target GMR frequency according to

$$\sqrt{\frac{(\omega_2 - \omega_1)^2}{(\omega_2 + \omega_1)^2} - \frac{(\omega_{\text{res}} - \omega_0)^2}{(\omega_0)^2}},$$
 (1)

where  $\omega_2$ ,  $\omega_1$  and  $\omega_0$  are, respectively, the frequencies for the air band edge, dielectric band edge and mid-gap frequency of the mirror

segment, and  $\omega_{\rm res}$  is the GMR frequency<sup>42</sup>. By tracking the positions of the dielectric (bonding mode) and air (anti-bonding mode) bands of mirror segments with varying widths (d), we determine their respective strengths (Fig. 2e and Supplementary Fig. 2). Based on these calculations, we opt for a segment with d = 2.5  $\mu$ m as the strongest and a segment with d = 600 nm as our weakest mirror segment.

Creating a Gaussian field envelope using rationally tapered mirrors minimizes radiation losses and maximizes mode confinement in photonic crystal cavities, as demonstrated by out-of-plane Fourier analyses<sup>29</sup>. To achieve a Gaussian field profile within our 15-um-long antenna, the width of each mirror segment (d) progressively increases from the cavity end to establish a polynomial taper, following  $X = AY^p + C$ . X gives the width of the mirror segment (d), Y represents the position of the mirror segment from the end of the cavity section, p indicates the polynomial's order, and A and C are constants dictated by the minimal and maximal widths of the mirror segments in the tapered mirrors section (detailed further in Supplementary Information). We arrange these mirror segments in an ascending order of strength within 5-µm-long tapered mirror sections on two ends of a 5-µm-long cavity. We examined seven distinct polynomial functions, from p = 0 to p = 6. We evaluated the mode confinement in the out-of-plane dimension by performing Fourier transforms (FT) of the cross-sectional electric near-field profile, to quantify radiation<sup>29,44</sup>. Figure 2f displays a cross-sectional near-field representation of the x component of the electric field and its corresponding FT spectrum for an unperturbed VINPix resonator ( $\Delta d = 0$ ), with mirror sections exhibiting no taper (p = 0). In this instance, a pronounced intensity within the radiation zone is apparent, signifying substantial radiation losses. These losses result in a modest simulated Q factor of approximately 1,900. In contrast, Fig. 2g shows a VINPix resonator with a Q factor of ~615,000. Here, a mirror section employing a fourth-order polynomial taper generates a more Gaussian-like field envelope and a substantial decrease in intensity within the radiation zone (see Supplementary Fig. 5 for one-dimensional line traces). By employing rational taper functions for the mirror, we minimize radiative losses in our design.

# Optimization and measurements of high-Q VINPix resonators

We optimize our VINPix design with width perturbations in the cavity to maximize Q factors while retaining free-space excitation. Figure 3a shows simulated Q factors for a 15-μm-long VINPix with a 5-μm-long cavity and varying perturbation ( $\Delta d$ ), truncated by 5-um-long tapered mirror sections of different polynomial orders (p). A fourth-order polynomial taper yields the most optimal confinement for a range of perturbation magnitudes, consistent with simulations sans perturbations (Fig. 2g). Employing a fourth-order polynomial taper, we conduct a coarse optimization analysis to identify optimal length ratios for each section of the VINPix resonator (Fig. 3b). Note that, here, the padding section is a set of the strongest mirrors that can be added to the end of the tapered mirrors for increased confinement. We achieve calculated Q factors, exceeding 10,000 by configuring the VINPix resonator with a cavity length of 7-µm-long and 4-µm-long mirror sections (Fig. 3b). Figure 3c depicts the simulated normalized electric near-field intensity (log scale) at the cross-section of the optimized VINPix resonator design. Using this near-field profile, we calculated the far-field response, as seen in Fig. 3d. The VINPix shows a strong directional emission in the primary resonance mode (Supplementary Fig. 6). Figure 3e is a cross-sectional x-z near-field profile at the GMR wavelength. Our simulations result in a refined 15-µm-long, high-Qantenna with a dipole-like far-field pattern and reduced higher-order radiation.

We validate our resonator design using a home-built reflection microscope (detailed in Methods and Supplementary Fig. 7). Guided by our calculations, we opt for a 7- $\mu$ m-long cavity section and 4- $\mu$ m-long tapered mirrors. We fabricate and characterize individual resonators with varied polynomial orders (from p=1 to 6) and perturbations ( $\Delta d=50$  nm and 100 nm). Figure 3f shows a SEM image of

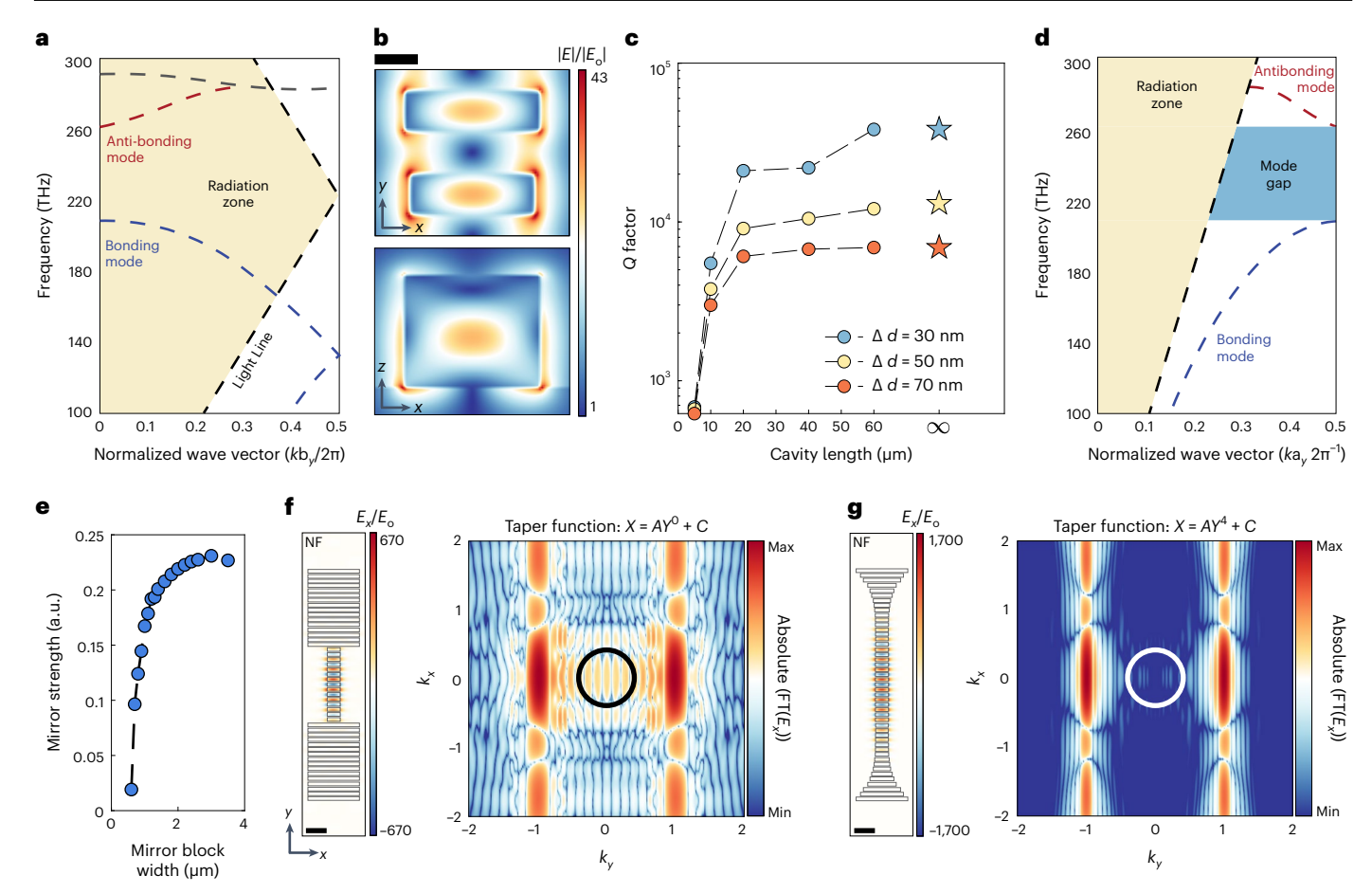


**Fig. 2**| **Photonic mirrors confine GMRs. a**, Simplified TE band diagram of infinitely long photonic cavity with average width, d=600 nm, and  $\Delta d=50$  nm, the unit cell size  $(b_y)=660$  nm. Bands at 207 THz and 262 THz (for  $k_{\parallel}=0$ ) are the bonding and anti-bonding GMRs of interest. Refer to Supplementary Fig. 1 for a schematic of our waveguide cavity and band diagram calculations. **b**, Simulated normalized electric field enhancements at the cross-section of the unit cell of an infinitely long cavity with  $\Delta d=50$  nm, of the bonding GMR. Geometrical parameters of the unit cell are: height of 600 nm, average width (d)=600 nm, thickness (t)=160 nm and block spacing  $(a_y)=330$  nm. Scale bar, 200 nm. The colour bar is linearly scaled. **c**, Simulated Q factors of the GMR for waveguide cavities of different lengths. The stars correspond to waveguide cavities of infinite length. **d**, Simplified TE band diagram for a mirror segment

with d=600 nm with labelled radiation zone, the bonding and anti-bonding modes, and the corresponding mode gap. Simulated mode profiles of the bonding and anti-bonding modes are shown in Supplementary Fig. 1. **e**, Mirror strength calculated using band positions. Refer to Supplementary Fig. 2 for band positions of the bonding mode (dielectric band edge), anti-bonding mode (air band edge) and the mid-gap frequency for different mirror segments. **f**,**g**, (left) Simulated cross-sectional field profiles for the x component of the electric field (colour bar is linearly scaled) and (right) corresponding FT spectra (colour bar is logarithmically scaled) to visualize the out-of-plane scattering for a VINPix with  $\Delta d=0$ , with a tapered mirrors section of p=0 (**f**) and p=4 (**g**). The region inside the circle is the radiation zone. Nanoblocks are marked with black borders to aid visualization. Scale bar,  $1 \, \mu \text{m}$ . NF stands for near-field.

a representative section of an array of 15-µm-long VINPix resonators. Figure 3g presents a spectral image from five individual VINPix resonators demonstrating that our high-Q GMRs do not rely on interdevice coupling. This makes each VINPix individually addressable enabling higher packing densities, exceeding millions per cm². The characterized GMR wavelength matches our theoretical predictions (detailed in Supplementary Fig. 8). Figure 3h presents Q factors obtained from this experiment. We observe the highest confinement with a fourth-order polynomial, as anticipated from simulations. Experimentally, we achieve Q factors peaking at ~4,700 (mean of ~3,500) with  $\Delta d$  = 50 nm, and ~2,000 (mean of ~1,600) with  $\Delta d$  = 100 nm for individual VINPix resonators. We also demonstrate the fabrication and characterization of VINPix resonators with different device spacings (3, 5, 7, and 9 µm) indicating that our resonators maintain high performance and minimal cross-coupling, even when densely packed (Supplementary Fig. 9).

Inspired by recent large-scale spatio-temporal light modulators and active metasurfaces  $^{8,13,16,17}$ , we fabricated an  $8 \text{ mm} \times 8 \text{ mm}$  VINPix array on a  $10 \text{ mm} \times 10 \text{ mm}$  chip, demonstrating scalability (Figs. 1g and 3i). Characterization across the array (Fig. 3j) shows Q factor and resonance wavelength variations from centre to periphery, attributed

to fabrication variances (Fig. 3k). Despite this variability, the VINPix array's overall performance remains robust, underscoring its potential for large-scale applications.

# Spatial refractive index mapping on a VINPix array

We fabricated a VINPix array to showcase potential applications in high-density, multiplexed computational spectrometry and biosensing, among others. Here, each VINPix reports the local refractive index via its spectral resonance shift, which we record via spatially dependent intensity variations. As illustrated in Fig. 4a, we use hyperspectral imaging to concurrently extract spectral and spatial data of individual VINPix resonators. This is achieved through a time series of wide-field images captured on a two-dimensional charge-coupled device (CCD) array, forming a data cube<sup>4</sup>. We pattern the top layer of 126 VINPix resonators with PMMA resist in the shape of an 'S'. Inside the 'S' is water (refractive index -1.33), while outside the 'S' is PMMA resist (refractive index -1.47) as shown in Fig. 4c,d (see Methods for details). We illuminate the VINPix array with a narrow-linewidth NIR tunable laser and sweep the wavelength from 1,560 nm to 1,620 nm

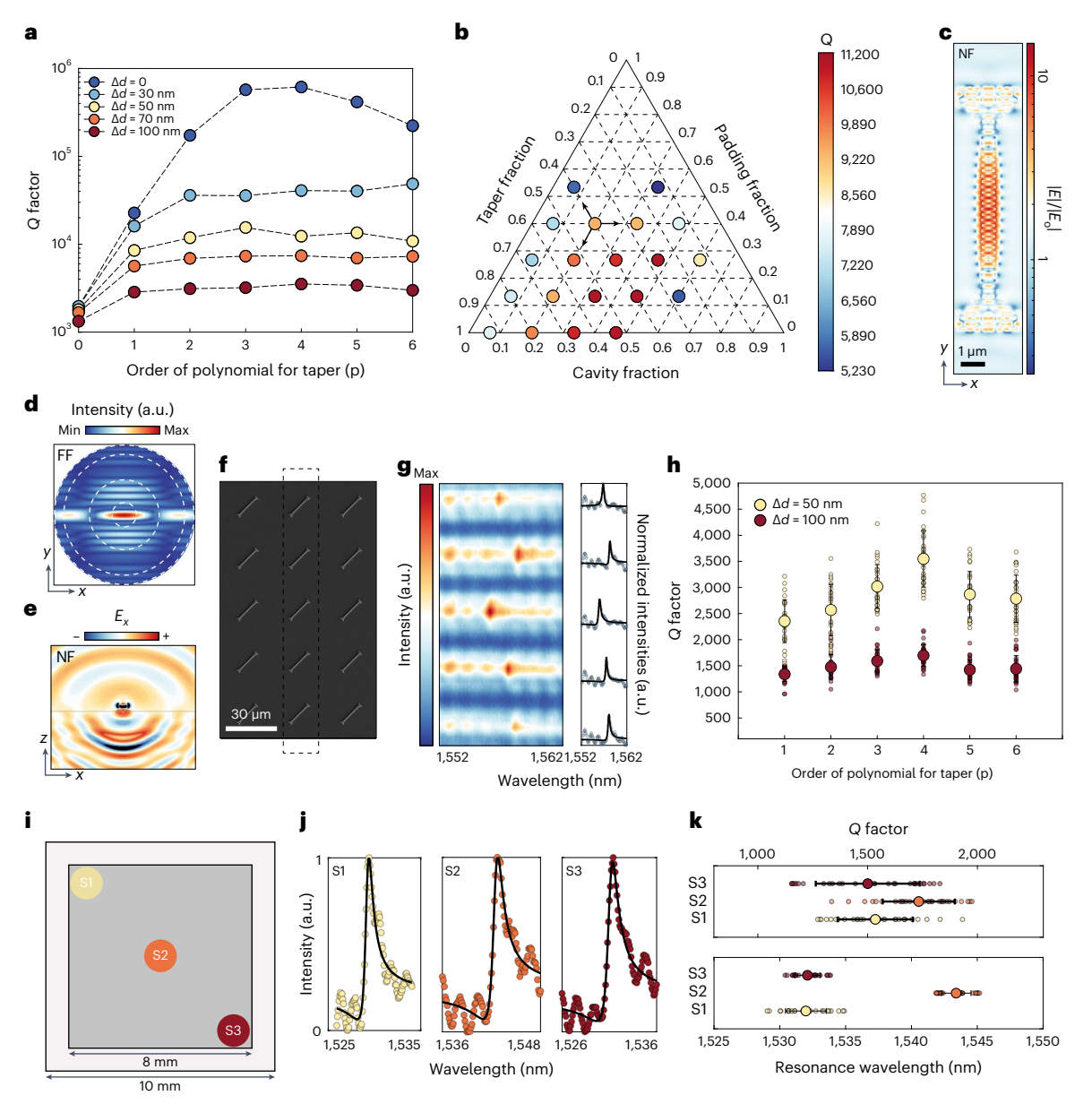


**Fig. 3** | **Optimization and characterization of VINPix resonators. a**, Simulated Q factors of 15-μm-long VINPix with a 5-μm-long cavity of different ( $\Delta d$ ) and 5-μm-long mirror sections of different p. **b**, Simulated Q factors of 15-μm-long VINPix with varying fractional configurations of the cavity sections', tapered mirror sections' (p=4) and padding mirror sections' lengths. The arrows point towards the respective axes for one representative configuration. **c**, Simulated normalized electric near-field (NF) enhancements at the cross-section of a VINPix with 7-μm-long cavity section of  $\Delta d=50$  nm, 3-μm-long mirror sections of p=4 and 1-μm-long padding sections. The colour bar is logarithmically scaled. **d**, Far-field (FF) simulation plot of the optimized VINPix. The concentric circles represent  $10^\circ$ ,  $30^\circ$ ,  $60^\circ$  and  $90^\circ$  from the centre. The colour bar is linearly scaled. **e**, Simulated electric near-field (NF) profile through the cavity of the optimized VINPix. Colour bar is linearly scaled. **f**, Representative SEM image of an array of 15-μm-long VINPix with p=4 and  $\Delta d=50$  nm. **g**, Spectral image from five

individual VINPix as marked in **f** (left) and normalized row-averaged reflected intensities corresponding to each VINPix (right). The colour bar is linearly scaled. **h**, Experimentally characterized Q factors of 15-µm-long VINPix with 7-µm-long cavity sections of  $\Delta d=50$  nm and 100 nm, and 4-µm-long tapered mirror sections of different polynomial orders. Average values and standard deviations (represented with error bars) correspond to 30 VINPix resonators measured for each set. **i**, Schematic of a VINPix array patterned with VINPix resonators  $(\Delta d=100$  nm) spanning an area of 8 mm  $\times$  8 mm on a 10 mm  $\times$  10 mm sapphire substrate. Resonators are spaced by 30 µm. **j**, Representative reflection spectra from individual resonators selected from the three regions of the chip—S1, S2 and S3 as marked and colour coded in **i**. **k**, Top: averaged Q factor values and standard deviations (represented with error bars) recorded across 30 resonators for each section. Bottom: averaged resonance wavelengths and standard deviations (represented with error bars) recorded across 30 resonators for each section.

in 0.05 nm increments. Each image frame corresponds to a single illumination wavelength as schematically shown in Fig. 4a,b. By sweeping the illumination wavelength across the resonances, we simultaneously image and collect spectra for hundreds of individually addressable resonators in a single experiment (Fig. 4e).

We extract the spectral information for each resonator as schematically shown in Fig. 4a,b. Here,  $R_{PMMA}$  is a VINPix situated outside

the 'S', while  $R_{\rm water}$  is located within the 'S'. The detected resonance wavelengths at ~1,570 nm ( $\lambda_{\rm water}$ ) and ~1,610 nm ( $\lambda_{\rm PMMA}$ ) for the two resonator groups agree with our theoretical calculations (Supplementary Fig. 10). As anticipated, the resonance wavelength for VIN-Pix resonators enveloped by PMMA is longer, attributable to the higher effective refractive-index of the encompassing medium. A spatially resolved map of resonance shifts spanning the entire field

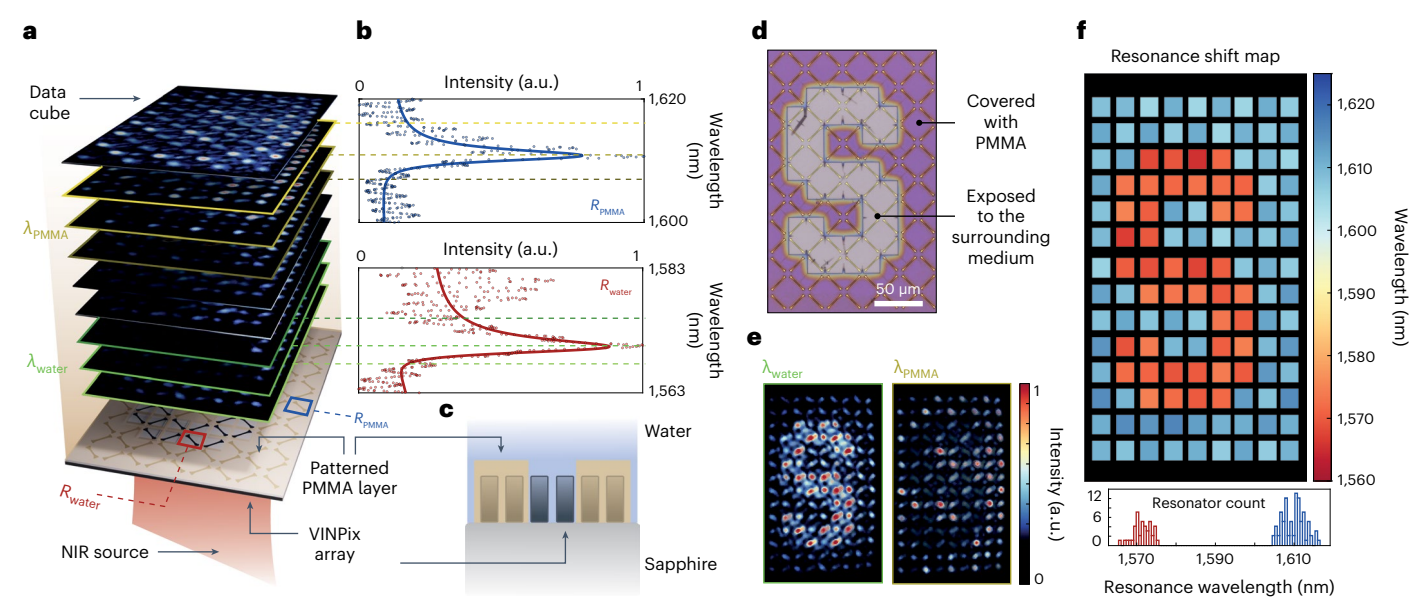


**Fig. 4** | **Sensing changes in the local refractive index using high-resolution hyperspectral imaging. a**, Schematic of our hyperspectral imaging setup. A VINPix array patterned with a PMMA layer on top in the shape of an 'S' is illuminated using a normally incident narrow band tunable NIR light source and the reflected images are recorded on a camera. **b**, Extracted spectral data corresponding to  $R_{\text{PMMA}}$  and  $R_{\text{water}}$  is shown with a VINPix resonator outside and inside the 'S', respectively. **c**, Schematic of the PMMA patterned array where certain VINPix structures are covered under PMMA. **d**, Optical microscopic image of the VINPix array after patterning a PMMA layer in the shape of the 'S' where the

resonators inside the 'S' are exposed to the top medium and the rest are covered under PMMA resist. **e**, Image frames recorded on the camera at the two resonance wavelengths where  $\lambda_{\text{water}}$  corresponds to -1,570 nm for GMR wavelengths of VINPix inside the 'S' and  $\lambda_{\text{PMMA}}$  corresponds to -1,610 nm for GMR wavelengths of VINPix outside the 'S'. Colour bar is linearly scaled. **f**, Top: spatial resonance-shift map generated by extracting spectral information for all the 126 VINPix resonators recorded in the data cube. Bottom: histogram displaying the GMR wavelengths of all the recorded VINPix resonators.

of view is shown in Fig. 4f. The appended histogram shows the GMR wavelengths for all VINPix resonators recorded in the experiment (Fig. 4f).

# Higher spatial confinement and sensitivity via a slot

We further decrease the  $V_{\rm m}$  of our VINPix resonators by incorporating a slot. Slotted photonic crystal cavities have shown extremely small mode volumes on the order of  ${\sim}0.01 (\lambda/n_{\rm air})^3$  (ref. 45). Due to electromagnetic boundary conditions, this secondary level of spatial localization mandates the field, formerly confined within the dielectric, to now concentrate within the air section, while maintaining the high-Q character  $^{46-48}$ .

To calculate the  $V_m$ , we use the conventional definition wherein  $V_m$  is determined using the electric field intensity (E) and permittivity ( $\varepsilon$ ):

$$V_{\rm m} = \frac{\int \epsilon |E|^2 dV}{\max(\epsilon |E|^2)}$$
 (2)

Introducing a slot (Fig. 5a, schematic and Fig. 5c, SEM image) reduces  $V_{\rm m}$ , but still retains relatively high Q factors. Figure 5b compares the theoretically calculated effective  $V_{\rm m}$  values for different device lengths of our waveguide cavity, VINPix design, and slotted VINPix with a 30-nm-wide slot (see Supplementary Fig. 11 for similar comparisons of Q factors and  $Q/V_{\rm eff}$ ). The length ratios for the cavity, tapered mirror and padding mirror sections are kept the same across all different device lengths using highest Q factor configuration ratio from our optimizations (Fig. 3b). Our VINPix resonators exhibit  $V_{\rm m}$  values close to  $1(\lambda/n_{\rm eff})^3$  and as small as  $\sim 0.07(\lambda/n_{\rm air})^3$  after introducing a 30-nm-wide slot. Here,  $n_{\rm eff}$  is 2.24, the average of the refractive indices of air and Si based on our waveguide cavity's design, and is used to calculate the effective  $V_{\rm m}$  for both the waveguide cavity and VINPix designs. For the slotted VINPix design, the field confinement is at a maximum within the air slot, so  $n_{\rm eff} = n_{\rm air} = 1$  in that case. Figure 5d

illustrates the normalized cross-sectional electric field intensity of a 15- $\mu$ m-long slotted VINPix with a 30-nm-wide slot, showing an electric field enhancement of approximately 110-fold within the slot—substantially higher than our infinitely long waveguide cavity (-40-fold; Fig. 2b) and a VINPix resonator without a slot (-10-fold; Fig. 3c). Figure 5e shows the electric field enhancements of a smaller region at the centre of the VINPix.

In Fig. 5f, we compare experimentally measured Q factors (circles) of slotted VINPix to theoretical predictions (stars). Measurements were made on 15-um-long slotted VINPix resonators with p = 4 and slots 70 nm and 100 nm wide. Both simulations and experiments exhibit a decrease in the O factor compared with a VINPix resonator (from an average of ~3,500 to ~1,600) as the field is now localized within a lower refractive index medium. Nevertheless, while Q factor decreases by ~2.2-fold,  $V_{\rm m}$  shrinks by ~100-fold in simulations, boosting the effective  $Q/V_{\text{eff}}$  ratio substantially (Supplementary Fig. 11). Higher  $Q/V_{\text{eff}}$  and more accessible enhanced electric fields increase the sensitivity of our slotted VINPix design (Fig. 5g). The resonator's sensing figure of merit is defined as sensitivity (resonant wavelength shift per refractive index unit (RIU) change) divided by the full width at half maximum of the mode. We observe higher resonant wavelength shifts per RIU change with our slotted VINPix resonators compared with those without the slots (see Supplementary Fig. 12 for simulated results and comparison with other designs). With high-Q factors and subwavelength  $V_{\rm m}$ , our optimized slotted VINPix design achieves an excellent figure of merit (FOM) of ~440 nm RIU<sup>-1</sup> with effortless free-space excitation and efficiently captured controlled radiation. Notably, while ensemble sensitivity sees an averaged response manifested by the radiating field in the vicinity of the resonators, a single or few molecules adeptly placed in the slot region of high electromagnetic intensity would experience a much more pronounced interaction. Hence, for sparse-molecule measurements in the slot, the sensitivity enhancement is expected to be substantially greater.

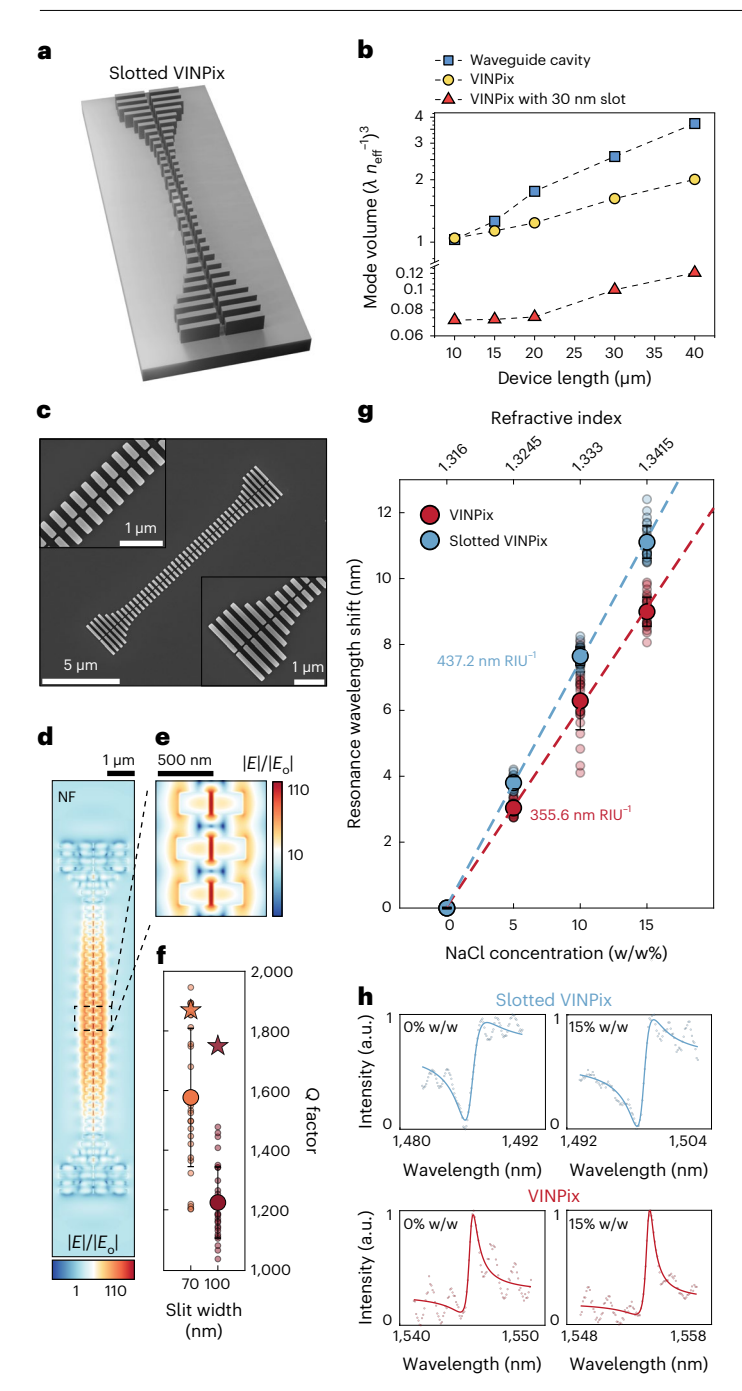


Fig. 5 | Slots boost light confinement within our VINPix resonators.  $\pmb{a}, Schematic of a slotted VINPix. \pmb{b}, A comparison of simulated effective$ mode volumes for our perturbed waveguide cavity, optimized VINPix, and a slotted VINPix with a 30-nm-wide slot. c, Top-down SEM images of a slotted VINPix with insets showing the cavity and mirror sections. d, Simulated normalized electric field enhancements at the cross-section of a 15-um-long slotted VINPix with a 30-nm-wide slot. The colour bar is logarithmically scaled. NF, near field. e, Zoomed-in normalized electric field enhancements of a small region at the centre of the VINPix. The colour bar is logarithmically scaled. f, Simulated (stars) and experimentally characterized (circles) Q factors of slotted VINPix with 70-nm-wide and 100-nm-wide slots. Average values and standard deviations (represented with error bars) correspond to 30 slotted VINPix resonators measured for each set. g, Resonant wavelength measurements as a function of background medium refractive index with slotted VINPix. Average values and standard deviations (represented with error bars) correspond to 30 resonators measured for each set. The lines represent linear fits to the data. h, Spectra of characterized representative VINPix with and without slots at 0 and 15% NaCl concentrations.

## Conclusion

We introduce high-O photonic nanoantennas-VINPix-that integrate key features of high-O GMR waveguides and tapered photonic crystal cavities. We simultaneously achieve high Q factors, subwavelength  $V_{\rm m}$ and controlled dipole-like radiation, with free-space coupling. We experimentally demonstrated average Q factors of ~3,500 in 15-µm-long VINPix resonators. We further sense local refractive index changes using high-resolution hyperspectral imaging using a dense VINPix array. The introduction of a slot increases the spatial localization of our resonator, enabling subwavelength volumes as low as  $\sim 0.07 (\lambda/n_{\rm air})^{3}$ and increased sensitivity to refractive index variations with an ROI of ~440 nm RIU<sup>-1</sup>. The slotted VINPix design enhances the local electromagnetic field strength, which is promising for detecting molecules at concentrations lower than the femtomolar range based on our previous work<sup>7</sup> and potentially at the few-to-single molecule level. By employing surface functionalization<sup>7,49,50</sup>, nanofluidic strategies<sup>51-53</sup> and surface photochemistry with nano-scale spatial resolution<sup>54</sup>, one can selectively capture and interact with target molecules within the slots. Such selective strategies would substantially increase the detection sensitivity.

The strong localized field enhancement within the slots (~110×) also opens potential for applications beyond molecular sensing. For example, each antenna could act as an independent micro-reactor or thermal heater, facilitating large-scale chemical reactions at the nano-scale. Already, DNA synthesis for synthetic biology is conducted on optically addressable Si microarrays, and our VINPix resonators could facilitate higher-density, longer-oligo synthesis. VINPix arrays could also be configured to enhance vibrational (such as infra-red and Raman) scattering. Here, one could foresee VINPix arrays as substrates for high-efficiency, label-free chemical profiling of materials-from the tumour immune environment to battery electrodes. The individual addressability and decoupled nature of the resonators at high densities also allows for applications in spatio-temporal modulation, promising for beam steering, holography, and dynamic wavefront shaping. For these applications, addition of electrical interconnects will be crucial, yet tractable with standard complementary metal-oxide semiconductor-compatible processes.

Our devices are fully complementary metal-oxide semiconductor compatible, so foundry-scale fabrication of 200-300 mm wafers should be achievable. Here, attention must be given to bolster uniformity in VINPix dimensions, resonant wavelength and Q factor across the full wafer, nominally with <5% variation for key applications. With the capability to pattern millions of individually addressable resonators per square centimetre on large scales, the VINPix platform opens exciting avenues for developing innovative integrative and/or wearable and deployable photonic platforms for multiplexed health and environmental monitoring, molecular synthesis, enhanced vibrational spectroscopy, wavefront shaping and on-chip spectrometry.

## Online content

Any methods, additional references, Nature Portfolio reporting summaries, source data, extended data, supplementary information, acknowledgements, peer review information; details of author contributions and competing interests; and statements of data and code availability are available at https://doi.org/10.1038/s41565-024-01697-z.

## References

- Kuznetsov, A. I. et al. Roadmap for optical metasurfaces. ACS Photonics 11, 816–865 (2024).
- Chen, H.-T., Taylor, A. J. & Yu, N. A review of metasurfaces: physics and applications. Rep. Prog. Phys. 79, 076401 (2016).
- Lin, D., Fan, P., Hasman, E. & Brongersma, M. L. Dielectric gradient metasurface optical elements. Science 345, 298–302 (2014).
- Tittl, A. et al. Imaging-based molecular barcoding with pixelated dielectric metasurfaces. Science 360, 1105–1109 (2018).

- Zhang, S. et al. Metasurfaces for biomedical applications: imaging and sensing from a nanophotonics perspective. *Nanophotonics* 10, 259–293 (2021).
- Tseng, M. L., Jahani, Y., Leitis, A. & Altug, H. Dielectric metasurfaces enabling advanced optical biosensors. ACS Photonics 8, 47–60 (2021).
- Hu, J. et al. Rapid genetic screening with high quality factor metasurfaces. Nat. Commun. 14, 4486 (2023).
- Zhang, X., Kwon, K., Henriksson, J., Luo, J. & Wu, M. C. A large-scale microelectromechanical-systems-based silicon photonics LiDAR. *Nature* 603, 253–258 (2022).
- Li, N. et al. Spectral imaging and spectral LIDAR systems: moving toward compact nanophotonics-based sensing. *Nanophotonics* 10, 1437–1467 (2021).
- Chen, W. T., Zhu, A. Y., Sisler, J., Bharwani, Z. & Capasso, F. A broadband achromatic polarization-insensitive metalens consisting of anisotropic nanostructures. *Nat. Commun.* 10, 355 (2019).
- Lawrence, M. et al. High quality factor phase gradient metasurfaces. Nat. Nanotechnol. 15, 956–961 (2020).
- 12. Jang, M. et al. Wavefront shaping with disorder-engineered metasurfaces. *Nat. Photonics* **12**, 84–90 (2018).
- 13. Rogers, C. et al. A universal 3D imaging sensor on a silicon photonics platform. *Nature* **590**, 256–261 (2021).
- Colburn, S., Zhan, A. & Majumdar, A. Metasurface optics for full-color computational imaging. Sci Adv 4, eaap9956 (2018).
- Arbabi, A., Horie, Y., Bagheri, M. & Faraon, A. Dielectric metasurfaces for complete control of phase and polarization with subwavelength spatial resolution and high transmission. *Nat. Nanotechnol.* 10, 937–943 (2015).
- Li, S.-Q. et al. Phase-only transmissive spatial light modulator based on tunable dielectric metasurface. Science 364, 1087–1090 (2019).
- 17. Panuski, C. L. et al. A full degree-of-freedom spatiotemporal light modulator. *Nat. Photonics* **16**, 834–842 (2022).
- Zangeneh-Nejad, F., Sounas, D. L., Alù, A. & Fleury, R. Analogue computing with metamaterials. Nat. Rev. Mater. 6, 207–225 (2020).
- 19. Silva, A. et al. Performing mathematical operations with metamaterials. *Science* **343**, 160–163 (2014).
- Gao, L., Qu, Y., Wang, L. & Yu, Z. Computational spectrometers enabled by nanophotonics and deep learning. *Nanophotonics* 11, 2507–2529 (2022).
- Wang, Z. et al. Single-shot on-chip spectral sensors based on photonic crystal slabs. *Nat. Commun.* 10, 1020 (2019).
- Cihan, A. F., Curto, A. G., Raza, S., Kik, P. G. & Brongersma, M. L. Silicon mie resonators for highly directional light emission from monolayer MoS<sub>2</sub>. Nat. Photonics 12, 284–290 (2018).
- Benea-Chelmus, I.-C. et al. Gigahertz free-space electro-optic modulators based on mie resonances. Nat. Commun. 13, 3170 (2022).
- Kuznetsov, A. I., Miroshnichenko, A. E., Brongersma, M. L., Kivshar, Y. S. & Luk'yanchuk, B. Optically resonant dielectric nanostructures. *Science* https://doi.org/10.1126/science.aag2472 (2016).
- 25. Schuller, J. A. et al. Plasmonics for extreme light concentration and manipulation. *Nat. Mater.* **9**, 193–204 (2010).
- Koshelev, K. et al. Subwavelength dielectric resonators for nonlinear nanophotonics. Science 367, 288–292 (2020).
- Barton, D. et al. High-Q nanophotonics: sculpting wavefronts with slow light. Nanophotonics 10, 83–88 (2021).
- 28. Overvig, A. C., Shrestha, S. & Yu, N. Dimerized high contrast gratings. *Nanophotonics* **7**, 1157–1168 (2018).
- Akahane, Y., Asano, T., Song, B.-S. & Noda, S. High-Q photonic nanocavity in a two-dimensional photonic crystal. *Nature* 425, 944–947 (2003).

- Hu, S. & Weiss, S. M. Design of photonic crystal cavities for extreme light concentration. ACS Photonics 3, 1647–1653 (2016).
- Miura, R. et al. Ultralow mode-volume photonic crystal nanobeam cavities for high-efficiency coupling to individual carbon nanotube emitters. *Nat. Commun.* 5, 5580 (2014).
- 32. Altug, H., Englund, D. & Vučković, J. Ultrafast photonic crystal nanocavity laser. *Nat. Phys.* **2**, 484–488 (2006).
- Tanabe, T., Notomi, M., Kuramochi, E., Shinya, A. & Taniyama, H.
   Trapping and delaying photons for one nanosecond in an ultrasmall high-Q photonic-crystal nanocavity. *Nat. Photonics* 1, 49–52 (2006).
- 34. Matsko, A. B. & Ilchenko, V. S. Optical resonators with whispering-gallery modes-part i: basics. *IEEE J. Sel. Top. Quantum Electron.* **12**, 3–14 (2006).
- Armani, D. K., Kippenberg, T. J., Spillane, S. M. & Vahala, K. J. Ultra-high-Q toroid microcavity on a chip. *Nature* 421, 925–928 (2003).
- Gorodetsky, M. L., Savchenkov, A. A. & Ilchenko, V. S. Ultimate Q of optical microsphere resonators. Opt. Lett. 21, 453–455 (1996).
- 37. Lin, G., Diallo, S., Henriet, R., Jacquot, M. & Chembo, Y. K. Barium fluoride whispering-gallery-mode disk-resonator with one billion quality-factor. *Opt. Lett.* **39**, 6009–6012 (2014).
- 38. Zhang, J., MacDonald, K. F. & Zheludev, N. I. Near-infrared trapped mode magnetic resonance in an all-dielectric metamaterial. *Opt. Express* **21**, 26721–26728 (2013).
- 39. Mirzapourbeinekalaye, B., Samudrala, S., Mansouree, M., McClung, A. & Arbabi, A. Free-space-coupled wavelength-scale disk resonators. *Nanophotonics* **11**, 2901–2908 (2022).
- Zeng, B., Majumdar, A. & Wang, F. Tunable dark modes in one-dimensional 'diatomic' dielectric gratings. Opt. Express 23, 12478–12487 (2015).
- Wang, S. S. & Magnusson, R. Theory and applications of guided-mode resonance filters. *Appl. Opt.* 32, 2606–2613 (1993).
- 42. Quan, Q., Deotare, P. B. & Loncar, M. Photonic crystal nanobeam cavity strongly coupled to the feeding waveguide. *Appl. Phys. Lett.* **96**, 203102 (2010).
- Zain, A. R., Johnson, N. P., Sorel, M. & De La Rue, R. M. Ultra high quality factor one dimensional photonic crystal/photonic wire micro-cavities in silicon-on-insulator (SOI). Opt. Express 16, 12084–12089 (2008).
- Srinivasan, K. & Painter, O. Momentum space design of high-q photonic crystal optical cavities. Opt. Express 10, 670–684 (2002).
- Seidler, P., Lister, K., Drechsler, U., Hofrichter, J. & Stöferle, T. Slotted photonic crystal nanobeam cavity with an ultrahigh quality factor-to-mode volume ratio. Opt. Express 21, 32468–32483 (2013).
- Hu, S. et al. Experimental realization of deep-subwavelength confinement in dielectric optical resonators. Sci. Adv. 4, 2355 (2018).
- Almeida, V. R., Xu, Q., Barrios, C. A. & Lipson, M. Guiding and confining light in void nanostructure. Opt. Lett. 29, 1209–1211 (2004).
- 48. Choi, H., Heuck, M. & Englund, D. Self-similar nanocavity design with ultrasmall mode volume for single-photon nonlinearities. *Phys. Rev. Lett.* **118**, 223605 (2017).
- 49. Macchia, E. et al. Single-molecule detection with a millimetre-sized transistor. *Nat. Commun.* **9**, 3223 (2018).
- 50. Raveendran, M., Lee, A. J., Sharma, R., Wälti, C. & Actis, P. Rational design of DNA nanostructures for single molecule biosensing. *Nat. Commun.* **11**, 4384 (2020).

- Kovarik, M. L. & Jacobson, S. C. Nanofluidics in lab-on-a-chip devices. Anal. Chem. 81, 7133–7140 (2009).
- 52. Yamamoto, K., Ota, N. & Tanaka, Y. Nanofluidic devices and applications for biological analyses. *Anal. Chem.* **93**, 332–349 (2021).
- 53. Kim, S. J., Song, Y.-A. & Han, J. Nanofluidic concentration devices for biomolecules utilizing ion concentration polarization: theory, fabrication, and applications. *Chem. Soc. Rev.* **39**, 912–922 (2010).
- 54. Leggett, G. J. Scanning near-field photolithography-surface photochemistry with nanoscale spatial resolution. *Chem. Soc. Rev.* **35**, 1150–1161 (2006).

**Publisher's note** Springer Nature remains neutral with regard to jurisdictional claims in published maps and institutional affiliations.

Springer Nature or its licensor (e.g. a society or other partner) holds exclusive rights to this article under a publishing agreement with the author(s) or other rightsholder(s); author self-archiving of the accepted manuscript version of this article is solely governed by the terms of such publishing agreement and applicable law.

© The Author(s), under exclusive licence to Springer Nature Limited 2024

### Methods

#### Computational design

Simulations were performed using the Lumerical finite difference time domain (FDTD) solver (Lumerical 2023 R1.3). Perfectly matched layer boundary conditions in the x and y directions were used for structures with finite lengths. Perfectly matched layer boundary conditions were used in the z direction in all cases. Localized dipole sources were used to excite structures with no perturbations ( $\Delta d = 0$ ). For structures with non-zero perturbations ( $\Delta d \neq 0$ ), a plane wave excitation source was used in the case of periodic boundary conditions, whereas a total-field/scattered-field excitation source was used otherwise. The standard polarization used with all plane wave and total-field/ scattered-field sources in simulations was transverse electric (TE) polarization, where the electric field is along the x direction, considering that the antenna extends in length along y and the sapphire substrate/medium is along the z direction. The plane wave incidence is along the positive z direction. Default material options from Lumerical FDTD solver's database were used wherever possible. A mesh size of 10 nm × 10 nm × 10 nm was used to simulate structures featuring features of 50 nm or larger. Smaller mesh dimensions as small as 5 nm were used appropriately for smaller feature sizes. Simulated Q factors were calculated using Lumerical FDTD solver's high-Q analysis monitor. Consistent Q factors were observed with all three sources for waveguide cavities of different lengths (Supplementary Fig. 13). Standalone device simulations, for example, for VINPix optimizations, were performed in air as the medium. Simulations to replicate experimental results were performed in water as the medium. Far-field and k-space plots were calculated using the x component of the electric near-field from a monitor situated at the cross-section of our resonators.

#### **Fabrication**

Photonic structures were fabricated using standard lithographic procedures. Resonators were patterned at 45° with respect to the c axis of sapphire. This configuration helped in overcoming the birefringence of the sapphire substrate, which can otherwise introduce polarization-dependent variations in the measured signals. First, 600 nm, single-crystal silicon-on-sapphire (MTI Corporation and University Wafer) substrates were cleaned by rinsing with acetone, methanol and isopropanol, followed by sonication in acetone and isopropanol followed by a dehydration bake at 180 °C for 2 min. The substrates were spin-coated with hydrogen silsesquioxane (HSQ) negative tone resist (XR-1541-006, DuPont) at 1,500 RPM. The resist was baked for 5 min at 80 °C. To reduce charging, a charge dissipation layer (e-spacer, Showa Denko) was spin-coated at 2,000 RPM over the HSQ resist and baked again for 2 min at 80 °C. The patterns were defined using electron beam lithography (Raith Voyager) with a 50 kV accelerating voltage and developed in a solution consisting of 4% sodium chloride and 1% sodium hydroxide in water. After exposure and development, the patterns were transferred to the chip using reactive ion etching (Oxford III-V Etcher) using HBr and Cl<sub>2</sub> chemistry for an anisotropic silicon etch. Lastly, the resist was removed using 2% hydrofluoric acid in water, followed by cleaning in a Piranha solution at 120 °C to remove any organic residue. Further, for preparing the VINPix array for hyperspectral imaging, patterned silicon-on-sapphire array was cleaned by rinsing with acetone, methanol and isopropanol, followed by sonication in acetone and isopropanol, followed by a dehydration bake for 2 min. The metasurface was spin-coated with PMMA 950A4 positive resist at 3,000 RPM, followed by a 2 min bake at 110 °C. A charge dissipation layer (e-spacer, Showa Denko) was spin-coated at 2,000 RPM over the PMMA resist and baked again for 2 min at 110 °C. The PMMA patterns were defined using electron beam lithography (Raith Voyager) with a 50 kV accelerating voltage and developed in a solution consisting of a 1:3 ratio of methyl isobutyl ketone and isopropanol.

#### SEM characterization

Representative images were taken using a FEI Magellan 400 XHR scanning electron microscope with a field emission gun source. A representative sample was coated with a -5 nm film of Au to reduce charging. For side and tilted views, the stage was titled by 30°. Images were typically acquired with an accelerating voltage of 5–10 kV.

#### **Optical characterization**

Resonator spectra were measured in a home-built NIR reflection microscope shown in Supplementary Fig. 7. Samples were illuminated via a broadband super-continuum laser (NKT SuperK EXTREME) or a tunable narrow-linewidth laser (SANTEC TSL-550), with a collimated fibre output. A polarizer P1 was set to create linearly polarized incident illumination at a 45° angle with respect to the metasurface resonators. The illuminating beam was focused on the back focal plane of an objective (Mitutoyo Plan Apochromat NIR) with a lens L1 (f = 75 mm or f = 100 mm) to produce a collimated plane wave at the sample. The devices were illuminated through the sapphire substrate. To demonstrate general applicability, we characterized our VINPix metasurface under a droplet of water, following the common practice employed in biomolecular sensing. The scattered light was directed through a cross-polarized polarizer P2 at -45° to reduce the substrate Fabry-Pérot signal. The scattered light is then focused via a lens L2 (f = 75 mm) into a spectrometer (Princeton Instruments SPR-2300). The broadband signal is diffracted via a diffraction grating (600 g mm<sup>-1</sup>, blaze wavelength 600 nm, Princeton Instruments) and focused onto a TE cooled InGaAs CCD detector (NiRvana, Princeton Instruments). While using the SANTEC for hyperspectral imaging, the diffraction grating is eliminated, and the images are recorded straight on the InGaAs CCD detector. We employ a cross-polarization configuration to mitigate the Fabry-Pérot resonances and to minimize background signal. This approach was crucial in ensuring that the measured signals were predominantly from the VINPix resonators themselves, rather than being confounded by substrate-related interference effects.

Throughout the paper, the measured resonant spectral features were first normalized and then analysed by fitting the diffraction efficiency data with the function

$$T = \left| \frac{1}{1 + F \sin^2(n_s k h_s)} \right| \left| a_r + a_i i + \frac{b}{f - f_0 + i \gamma} \right|^2$$
 (3)

The first term accounts for the Fabry–Pérot interference through the substrate of thickness  $h_s$  and refractive index  $n_s$ . k is the free-space wavevector  $\left(\frac{2\pi}{\lambda}\right)$  and F accounts for the reflectivity of the interfaces. The second term represents the superposition between a constant complex background,  $a_r+a_i i$ , and a Lorentzian resonance with resonant frequency  $(f_0)$  and full width at half maximum  $(2\gamma)$ . The Q factor of this resonance is calculated as  $Q=\frac{f_0}{2\gamma}$ .

#### Analysis of hyperspectral data cube

Each image frame in the hyperspectral data cube corresponds to a single illumination wavelength. A time series of wide-field image frames representing intensity mappings were collapsed by uniform summation into a singular frame to locate VINPix centres. Pixel rows and columns corresponding to maximum intensity in the image frames were selected by determining peaks via local maxima, and manual adjustments were made on the basis of physical VINPix spacing constraints to remove spatial overlap. VINPix centres were then assigned and labelled at each row and column cross-section. Because our VINPix size is greater than the individual pixels of our CCD camera, a  $9 \times 9$  pixel intensity integration centred at our VINPix centres was performed for each frame in the hyperspectral stack. Spectral features were then extracted from each VINPix region and fitted to a Fano lineshape using the above-mentioned formula (3).

# Data availability

The data that support the plots and other findings in the work are available in the article and the supplementary information file, and are available from the corresponding authors on reasonable request.

# **Code availability**

The source code for the calculations conducted in this study is available from the corresponding authors on reasonable request.

# **Acknowledgements**

The authors thank D. McCoy, F. Pan, B. Bourgeois and A. Dai for insightful discussions. The authors acknowledge funding from a NSF Waterman Award (grant number 1933624), which supported the salary of J.A.D.; the MURI (grant number NO0014-23-1-2567), which supported the chip design, fabrication and salary of V.D. and S.D.; and the US Department of Energy, Office of Basic Energy Sciences (DE-SC0021984), which supported the chip characterization and salary of S.A. and H.C.D. V.D. was additionally supported by the Office of the Vice Provost for Graduate Education at Stanford through the Stanford Graduate Fellowship in Science and Engineering. H.B.B. acknowledges support from the NSF OCE-PRF (grant number: 2205990), the HHMI Hanna H. Gray Fellowship and the Stanford Sustainability Accelerator. S.D. was additionally supported by the Department of Defense (DOD) through the National Defense Science and Engineering (NDSEG) Fellowship Program. Part of this work was performed in part in the nano@Stanford labs, which are supported by the National Science Foundation as part of the National Nanotechnology Coordinated Infrastructure under award ECCS-2026822. Part of this work was performed at the Stanford Nano Shared Facilities (SNSF), supported by the National Science Foundation under award ECCS-2026822.

#### **Author contributions**

V.D., J.H., M.L. and J.A.D. conceived and designed the experiments. V.D. conducted the theory and numerical simulations. V.D., S.D., S.A., H.C.D. and P.M. fabricated the nanostructured samples. V.D., H.B.B. and S.D. performed the optical characterization experiments. V.D. and K.C. analysed the collected experimental data. A.S., F.S. and V.D. conducted the scanning electron microscopic characterizations. J.A.D. conceived the idea and supervised the project, along with M.L., J.H. and H.B.B. on relevant portions of the research. All authors contributed to the preparation of the manuscript.

# **Competing interests**

J.H., F.S. and J.A.D. are shareholders in Pumpkinseed Technologies, Inc. The remaining authors declare no competing interests.

## **Additional information**

**Supplementary information** The online version contains supplementary material available at https://doi.org/10.1038/s41565-024-01697-z.

**Correspondence and requests for materials** should be addressed to Varun Dolia, Mark Lawrence, Jack Hu or Jennifer A. Dionne.

**Peer review information** *Nature Nanotechnology* thanks Ho Wai Howard Lee, Vladimir Tuz and the other, anonymous, reviewer for their contribution to the peer review of this work.

**Reprints and permissions information** is available at www.nature.com/reprints.